

Towards balancing the oceanic Ni budget

S.H. Little^{1,2}, C. Archer³, J. McManus⁴, J. Najorka⁵, A. V. Wegorzewski⁶, D. Vance³

1. Department of Earth Sciences, University College London, Gower Place, London WC1E 6BS, UK.
2. Department of Earth Science and Engineering, Royal School of Mines, Imperial College London, London, SW7 2BP, UK.
3. Institute of Geochemistry and Petrology, Department of Earth Sciences, ETH Zürich, Clausiusstrasse 25, 8092 Zürich, Switzerland.
4. Bigelow Laboratory for Ocean Sciences, 60 Bigelow Drive, P.O. Box 380, East Boothbay, Maine 04544, USA.
5. Core Research Laboratories, The Natural History Museum, Cromwell Road, London SW7 5BD, UK.
6. Federal Institute for Geosciences and Natural Resources (BGR), Stilleweg 2, D-30655 Hannover, Germany.

Corresponding author: susan.little@ucl.ac.uk

For resubmission to: EPSL

3 June 2020

1 **Abstract**

2

3 Nickel isotopes are a novel and promising tracer of the chemistry of past ocean
4 environments, but realisation of this tracer's potential requires a comprehensive
5 understanding of the controls on Ni burial in the marine sedimentary archive. An
6 outstanding puzzle in the marine budget of Ni, first recognised in the 1970s, is a major
7 imbalance in the known inputs and outputs to and from the ocean: the sedimentary
8 outputs of Ni are much larger than the inputs (rivers, dust). Much more recently, it has
9 also been recognised that the outputs are also considerably isotopically heavier than
10 the inputs. In this study, we find light Ni isotope compositions ($\delta^{60}\text{Ni}_{\text{NIST SRM986}} = -0.2$
11 to -0.8‰) for Mn-rich sediments from the eastern Pacific compared to Fe-Mn crusts
12 (at about $+1.6\text{‰}$). These data suggest that diagenetic remobilisation of isotopically
13 heavy Ni leads to a significant benthic Ni flux (estimated at $0.6 - 2.3 \times 10^8$ mol/yr),
14 similar in magnitude to the riverine flux, to the ocean. Diagenetic remobilisation of Ni
15 may occur either via cycles of Mn-oxide dissolution and precipitation, with associated
16 Ni sorption and release, or during mineralogical transformation of birnessite to
17 todorokite. A minor role for retention of isotopically light Ni by Fe oxides or Fe-rich
18 authigenic clays is also proposed. Overall, a benthic flux of isotopically heavy Ni (at
19 about $+3\text{‰}$) can balance the marine Ni budget, pinpointing diagenesis as a key
20 missing piece of the Ni puzzle.

21

22

23

24 **1. Introduction**

25

26 Nickel is a cofactor in several enzyme systems central to the production of gases (CO₂,
27 CO, methane, ammonia, O₂, H₂) that are important to the carbon, nitrogen and oxygen
28 cycles (reviewed by Ragsdale, 2009). Nickel is utilised by marine phytoplankton as
29 the metal centre in urease, which catalyses the breakdown of urea to NH₃ and CO₂
30 (e.g., Price and Morel, 1991). A Ni-containing superoxide dismutase (Ni-SOD)
31 enzyme is also present in some marine plankton groups, used to detoxify reactive
32 oxygen species (e.g., Palenik et al., 2003). All methanogens have an obligate Ni
33 requirement due to the presence of several Ni containing enzymes, including methyl-
34 coenzyme M reductase (e.g., Jaun and Thauer, 2007). Methane may have played a key
35 role in maintaining a warm climate on the early Earth, leading to interest in the
36 development of Ni and its isotopes as a biomarker for methanogenesis (e.g., Cameron
37 et al., 2009; Wang et al., 2019).

38

39 The stable isotopes of Ni (reported as $\delta^{60/58}\text{Ni} = \left(\frac{{}^{60}\text{Ni}/{}^{58}\text{Ni}_{\text{sample}}}{{}^{60}\text{Ni}/{}^{58}\text{Ni}_{\text{SRM986}}} - 1\right) \times$
40 1000) could help to quantify and understand these issues in the past. However, the
41 development of a new isotope system as a tracer requires characterization of its
42 modern biogeochemical cycling. Indeed, stable isotope ratios provide useful
43 constraints on elemental global mass balances; that is, the input and output fluxes of
44 an element to and from the ocean. If we assume steady state, the Ni input and output
45 fluxes should balance (equation 1), as should their flux-weighted isotopic
46 compositions (equation 2):

47 (1) $F_{\text{input}} = F_{\text{output}}$

48
$$(2) F_{\text{input}}\delta_{\text{input}} = F_{\text{output}}\delta_{\text{output}}$$

49

50 where F_{input} and F_{output} are the respective input and output flux magnitudes, and δ_{input}
51 and δ_{output} their isotopic compositions. For our discussion here we assume that Ni is at
52 steady state over the past 10 – 20 kyr, i.e., on the timescale of the oceanic residence
53 time of Ni (Ciscato et al., 2018 this study).

54

55 Current best estimates of the inputs and outputs of Ni to and from the oceanic
56 dissolved pool are not in balance (Krishnaswami, 1976; Gall et al., 2013; Cameron and
57 Vance, 2014; Gueguen et al., 2016; Ciscato et al., 2018; Spivak-Birndorf et al., 2018).
58 The estimated total input of Ni to the ocean is approximately half of the total
59 sedimentary output fluxes. In addition, the known inputs are isotopically light (at
60 about +0.8‰; Cameron and Vance, 2014) compared to seawater (at about +1.4‰;
61 Archer et al., 2020; Cameron and Vance, 2014; Takano et al., 2017; Wang et al.,
62 2018), while most of the sedimentary outputs are isotopically similar to or heavier than
63 seawater (Gall et al., 2013; Gueguen et al., 2016; Ciscato et al., 2018). Balancing the
64 steady-state Ni budget either requires an isotopically heavy Ni input or an isotopically
65 light output flux, or both of these.

66

67 One key oceanic output flux of Ni is sorption to dispersed Fe-Mn oxide phases found
68 throughout oxygenated deep sea sediments, for which the isotopic composition of Fe-
69 Mn crusts has been used as a proxy (Cameron and Vance, 2014; Ciscato et al., 2018).
70 The Ni isotope composition of Fe-Mn crusts is variable, but generally similar to or
71 heavier than seawater, with average $\delta^{60}\text{Ni}_{\text{Fe-Mn crust}} = +1.62 \pm 0.37\text{‰}$ ($n = 28$; 1 SD,
72 Gall et al., 2013; Gueguen et al., 2016). Nickel is sorbed to the Mn oxide phase in Fe-

73 Mn crusts: specifically, to a poorly crystalline phyllomanganate of the birnessite
74 family (termed vernadite/ δ -MnO₂) (e.g., Koschinsky and Halbach, 1995; Koschinsky
75 and Hein, 2003; Peacock and Sherman, 2007a). However, sediments and Mn nodules
76 contain a mixture of vernadite and more crystalline 7Å and 10Å birnessite phases,
77 which transform to the tectomanganate phase todorokite during diagenesis (e.g., Burns
78 and Burns, 1979; Atkins et al., 2014). Recent experiments and the study of todorokite-
79 rich buried Mn nodules have shown that ~50% of sorbed Ni is released to the aqueous
80 phase during this mineralogical transformation (Atkins et al., 2016; Heller et al.,
81 2018). In addition, remobilization of Ni is observed in the Mn oxide reduction zone in
82 sub-oxic sediment porewaters (e.g., Klinkhammer, 1980; Heggie et al., 1986), where
83 ‘sub-oxic’ denotes low concentrations of both oxygen and sulphide. Either
84 transformation to todorokite or the reduction of Mn oxides may lead to a decreased Ni
85 trapping efficiency in sediments and a benthic return flux of Ni to seawater.

86

87 As yet, the potential for isotope fractionation during diagenetic Ni remobilization has
88 not been evaluated. We show that diagenesis significantly modifies the output flux of
89 Ni from the oceans, and infer a benthic return flux of isotopically heavy Ni. We
90 explore the extent to which this benthic flux can balance the oceanic Ni budget.

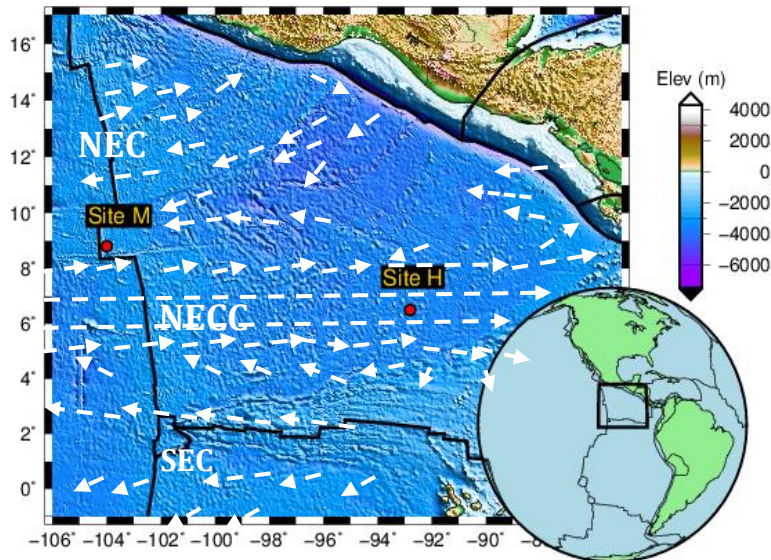
91

92 **2. Sites and Samples**

93

94 Metalliferous sediment samples were selected from two of the five MANOP
95 (Manganese nodule project) sites, M and H, both in the Guatemala Basin (Fig. 1).
96 Both sites are oxygenated at the sediment-water interface and sub-oxic below
97 (Klinkhammer, 1980). A surface nitrate maximum overlies a zone of Mn cycling, with

98 detectable porewater Mn at depths > 6 cm at Site M, and > 12 cm at Site H. Porewater
99 Fe is observed at depths > 13 cm at site M only (Fig. 3; Klinkhammer, 1980; Heggie et
100 al., 1986). Samples were collected using a 50 cm x 50 cm box corer and later sub-
101 sampled with a plastic core liner, using a piston to avoid core shortening. Five-six sub-
102 samples from the upper 20 cm of each core were included in this study.



103
104 **Figure 1.** Map of the Guatemala Basin showing the two MANOP site locations. Site
105 M is close to the East Pacific Rise, Site H is located on the flat plain of the Guatemala
106 Basin. Tectonic plate boundaries in black; surface ocean currents as white arrows
107 (NECC, North Equatorial Counter Current; NEC, North Equatorial Current; SEC,
108 South Equatorial Current) from Kessler (2006). Insert shows the location of the grid.
109

110 MANOP site M, chosen by MANOP to represent hydrothermal sedimentation, is
111 located 25 km east of the spreading axis of the East Pacific Rise, at 8.8°N 104.0° W,
112 ~3.1 km water depth (Fig. 1). The site is just 1,000 km away from the Central
113 American coast and within the source region of the westward flowing North
114 Equatorial Current (NEC). As a result, site M has a sedimentation rate of about 1
115 cm/1000 year (Kadko, 1981), with a combination of continental, hydrothermally-
116 derived, and biogenic sediment (at ~130 $\mu\text{g C}_{\text{org}}/\text{cm}^2\text{yr}$; Lyle et al., 1984). Surface

117 sediments at site M contain 10–40% calcium carbonate, 5–9% opal, and 1–2% organic
118 carbon (Lyle et al., 1984).

119

120 MANOP site H, the hemipelagic MANOP site, is located approximately 1,000 km east
121 of the East Pacific Rise on a relatively flat plain in the Guatemala Basin, at 6.5°N
122 92.8°W, ~3.6 km water depth. It lies at the northern edge of the eastward flowing
123 North Equatorial Counter-Current (NECC) and at the southwestern edge of the
124 productive Costa Rica Dome. The organic C flux at this site is similar to that at site M,
125 at ~110 $\mu\text{g C}_{\text{org}}/\text{cm}^2\text{yr}$ (Lyle et al., 1984). The site is currently at or just below the
126 calcite compensation depth, and the sedimentation rate, at ~0.65 cm/1000 yr, is about
127 half of that of site M due to greater dissolution of biogenic debris (carbonate) and the
128 lower quantity of continent-derived material (Kadko, 1981; Lyle et al., 1984).

129

130 Bulk samples of six well-characterized Mn nodule samples were also analysed for
131 their Ni isotope compositions in this study (Table 1). These include the two USGS
132 reference materials Nod P1 and Nod A1, one surface and two buried Fe-Mn nodules
133 from the Clarion-Clipperton Zone (CCZ) of the equatorial North Pacific (sites 21KG,
134 22KL; full details in: Heller et al., 2018; Wegorzewski et al., 2020) and one shallow
135 buried nodule from the Peru Basin (site 77BC). The selected surface and buried
136 nodules have evolved under differing redox regimes and are therefore compositionally
137 diverse, allowing comparisons to be made between phyllomanganate-rich and
138 todorokite-rich nodules (Table 1; Wegorzewski et al., 2020).

139

140 **Table 1.** Mn nodule samples studied, with predominant mineralogy as determined by
141 XRD analysis (Wegorzewski et al., 2020)

Mn Nodule	Location	Water depth/ Depth in sediment	Mineralogy
-----------	----------	-----------------------------------	------------

Nod A1	Atlantic 31°02'N 78°22'W	788 m / Surface	Phyllomanganates
Nod P1	Pacific 14°50'N 124°28'W	4300 m / Surface	Phyllomanganates
21KG-1n	CCZ, Pacific 13°10.529'N 118°08.187'W	4288 m/ Surface	Diagenetic growth structures: 7 and 10 Å phyllomanganates and hydrogenetic growth structures: vernadite (δ -MnO ₂) that is epitaxially intergrown with an amorphous FeOOH phase
77BC11-6	Peru Basin, Pacific 7°04.575' S 88°31.577' W	4130.5 m/ Shallowly buried	Mainly Todorokite
22KL-530cm	CCZ, Pacific 13°10.527'N 118°08.184'W	4302 m/ Deeply buried 530 cm	Mainly Todorokite, minor phyllomanganates
22KL-801cm	CCZ, Pacific 13°10.527'N 118°08.184'W	4302 m/ Deeply buried 801 cm	Mainly Todorokite, minor phyllomanganates

142

143 **3. Analytical Methods**

144

145 **3.1 MANOP mineralogy by XRD**

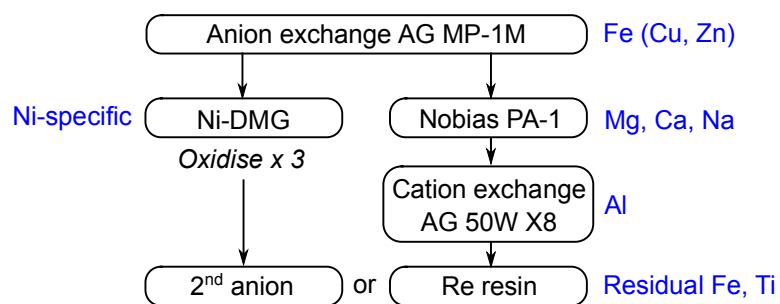
146 Selected samples from MANOP sites H and M (Table 2) were analysed by X-ray
147 diffractometry for their bulk mineralogy using a PANalytical X'Pert PRO instrument
148 at the Natural History Museum, London. Phase quantification was subsequently
149 attempted via a Rietveld refinement analysis of the 10 – 90° 2 θ region. Note that the
150 detection limit for the XRD analyses corresponds to about 1 – 5 wt%, depending on
151 the crystallinity and crystal symmetry of the phase (where a higher crystallinity and
152 crystal symmetry of a phase corresponds to a lower detection limit). For full details of
153 the XRD analyses, see the Supplementary Information.

154

155 **3.2 Element concentrations and Ni isotope ratios**

156 Bulk sample digestion was carried out in clean laboratories at ETH Zürich or Imperial
 157 College London, following previously published methods (Cameron and Vance, 2014;
 158 Vance et al., 2016; Ciscato et al., 2018; Archer et al., 2020). Between 20 and 100 mg
 159 of each sample was pre-digested by treatment with concentrated HNO₃ to attack
 160 carbonates, then completely digested in a 3:1 mixture of concentrated HF and HNO₃ -
 161 on a hotplate for 48 hours. Residual fluorides were removed by triplicate treatment
 162 with concentrated HNO₃, before final dissolution in 6 mL 7M HCl. Aliquots of these
 163 digest solutions were taken for multi-element analysis on a Thermo Element XR at
 164 ETH Zürich. Sub-samples were then spiked with a ⁶¹Ni–⁶²Ni double spike to achieve a
 165 sample-spike ratio of approximately 1 prior to column chromatography. Two different
 166 column chromatography procedures were utilised in this study, detailed in Figure 2
 167 and modified following Cameron and Vance (2014), Ciscato et al. (2018) and Archer
 168 et al. (2020). For full details, see the Supplementary Information.

169



171 **Figure 2.** Flowchart illustrating the two alternative Ni column chromatography
 172 procedures utilised in this study. Full details given in the Supplementary Information.

173

174 Nickel isotope compositions were analysed on a Neptune Plus multi-collector ICP-MS
 175 at ETH Zürich (Vance et al., 2016; Ciscato et al., 2018) and are reported relative to the
 176 NIST SRM986 Ni standard, as:

177

178 (2) $\delta^{60/58}\text{Ni} = \left(\frac{(^{60}\text{Ni}/^{58}\text{Ni})_{\text{sample}}}{(^{60}\text{Ni}/^{58}\text{Ni})_{\text{SRM 986}}} - 1 \right) \times 1000$

179

180 Accuracy and precision of the Ni isotope ratio measurements were monitored by
181 repeated analysis of the primary NIST solution standard at a range of sample:spike
182 ratios (0.2 to 5), and the repeated digestion and analysis of two reference materials,
183 USGS standards Nod P1 (+0.34 ± 0.05‰, 2SD, n = 5) and Nod A1 (+1.06 ± 0.02‰,
184 2SD, n = 5). The long-term reproducibility (± 0.07‰) was assessed by repeat
185 measurements of primary standards and one of the secondary standards, Nod A1
186 (digested and passed through the Ni column chemistry), the latter giving $\delta^{60}\text{Ni} = +1.04$
187 ± 0.07‰ (2 SD, n=175 over 4 years), in agreement with previously published results
188 (Gueguen et al., 2016).

189

190 **4. Results**

191

192 **4.1 Mineralogy and geochemistry**

193 The bulk mineral assemblages of the four MANOP samples analysed by XRD are
194 similar (Table S1, Figs S1-S4). The major mineral phase in all samples is smectite (49
195 – 60 wt%). Other minerals present in all samples include calcite (0.1 – 22 wt%),
196 plagioclase (13 – 20 wt%), quartz (4 – 6 wt%), halite (4 – 5 wt%), kaolinite (4 – 6
197 wt%) and barite (1 – 3 wt%). A Mn oxide phase, tentatively identified as birnessite, is
198 present at levels close to the detection limit of the XRD analysis (0.3 – 2 wt%).
199 Muscovite (4 wt%) is identified in the sample from site M (8967, 1–3 cm depth) only,
200 representing the only notable difference between this sample and the deepest sample at
201 site H (5313, 19–21 cm), which are otherwise similar in their phase quantification
202 (Table S1).

203

204 Elemental concentrations of the MANOP samples (Table 2, Table S2) are consistent
205 with the mineralogical information. Aluminium and Ti, expected to be present largely
206 in the silicate (i.e. clay mineral) fraction, are somewhat higher at site H (~5 and ~0.3
207 wt%, respectively) than site M (~4.2 and ~0.2 wt%), reflected in a higher proportion of
208 smectite at site H (Table S1). However, Fe concentrations are elevated at site M (~5.5
209 wt%) compared to site H (~4 wt%), and Fe/Al ratios at site M are significantly higher
210 than lithogenic values (e.g., upper continental crust, UCC; Fig. 3). Manganese
211 concentrations are high, particularly in the upper 10 cm at site H (at ~5 wt%),
212 dropping to ~2 wt% below this. The deepest sample at site M has a considerably lower
213 Mn content than the other samples, at 0.1 wt%.

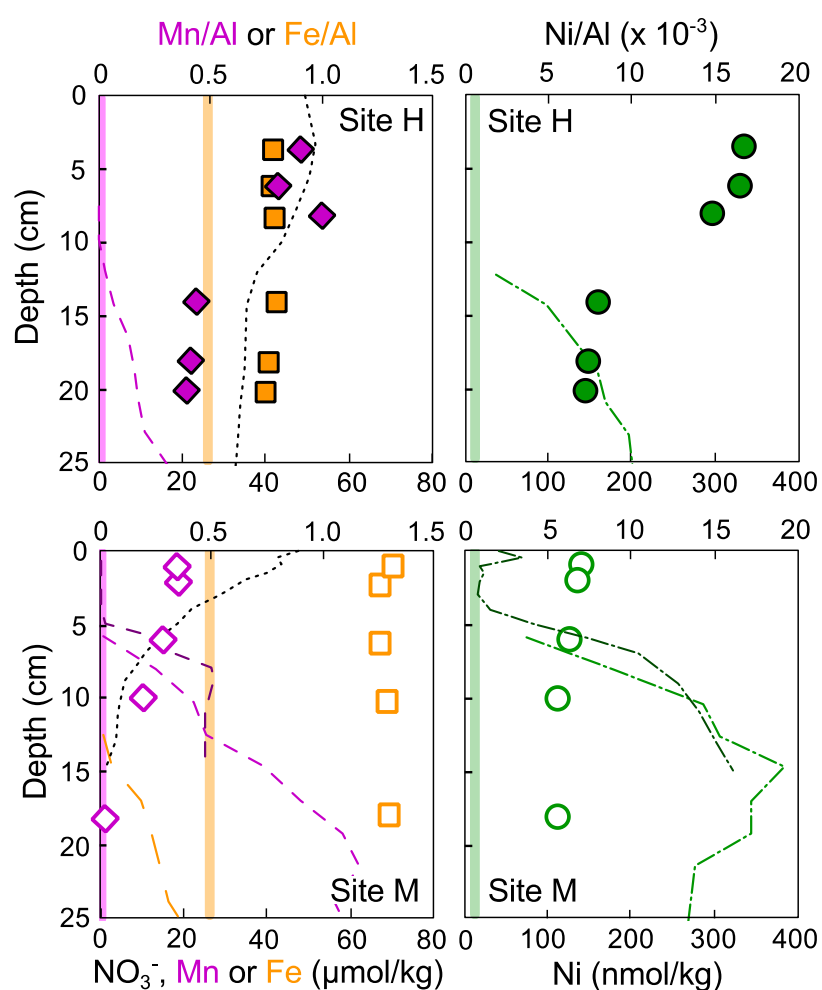
214

215 Trace metal concentrations (e.g., Ni, Cu, Zn, Mo, Cd), are significantly enriched at
216 both sites H and M relative to expected detrital abundances, e.g., as found in UCC
217 (Table 2, Table S2, Fig. 3), with enrichments typically greater at site H than at site M.
218 There is a coupling between Mn enrichment and those of Ni, Cu and Zn, particularly
219 clear at Site H, where the three shallowest samples (<10 cm depth) are considerably
220 more enriched than the three deeper samples (at 10 – 20 cm) (Fig. 3).

221

222 Manganese contents of Nod P1 and the CCZ surface and buried nodules are similar
223 (Table 2), at 31 to 32 wt%, while Fe contents are somewhat lower in buried nodules
224 (at ~3 wt%) than surface nodules (at 4 – 5 wt%). The Peru Basin nodule has an even
225 higher Mn content (at ~48 wt%). Nickel concentrations are highest in the Pacific
226 surface nodules (at ~1.1 wt%) and lower in the deeply buried nodules (at ~0.7–0.8
227 wt%). As a result, Ni/Mn ratios are lower in buried (~0.025) than surface (~0.038)

228 nodules. For a full discussion of the elemental distribution patterns in the CCZ
 229 nodules, see Heller et al. (2018). Atlantic Nod A1, which was collected from a much
 230 shallower water depth (776 m; Table 1) than the Pacific nodules, has a lower Mn
 231 content (20 wt%), a higher Fe content (10 wt%) and lower trace element
 232 concentrations (e.g., 0.6 wt% Ni, 0.1 wt% Cu), and an intermediate Ni/Mn ratio
 233 (0.029).
 234



235
 236 **Figure 3.** Solid-phase Mn/Al (purple diamonds), Fe/Al (orange squares), and Ni/Al
 237 (green circles) ratios in the sediment at the two MANOP sites. Filled symbols – site H,
 238 open symbols – site M. Solid coloured bars illustrate upper continental crust Me/Al
 239 ratios, from Rudnick and Gao (2003). Porewater concentrations of NO₃⁻ (black dotted
 240 lines), Mn (purple dashed lines), Fe (site M only, orange long dashed line) and Ni
 241 (green dot-dashed lines) from Klinkhammer (1980: Site H and M) and Heggie et al.

242 (1986; Site M only: darker coloured lines for Mn, Ni) are overlain on secondary x-
243 axes.

244

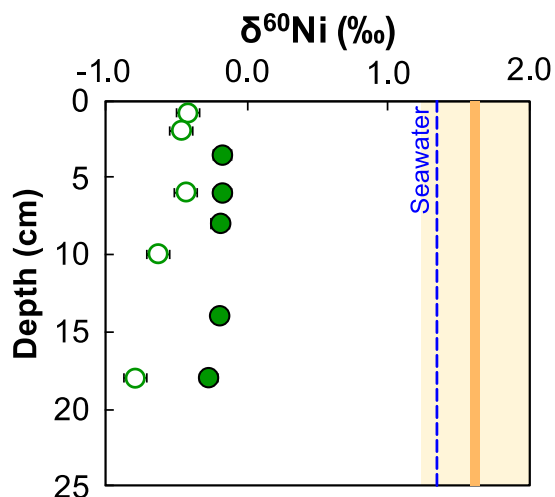
245

246 4.2 Ni isotope compositions

247

248 The Ni isotope compositions of samples from both MANOP sites are light relative to
249 seawater, ranging from -0.79 to -0.17‰ (Table 2; Fig. 4). $\delta^{60}\text{Ni}$ values for site H are
250 approximately homogeneous with depth, with mean $\delta^{60}\text{Ni}_H = -0.21 \pm 0.09\text{‰}$ (2 SD).
251 Site M $\delta^{60}\text{Ni}$ values are more negative than those of site H, and become isotopically
252 lighter with depth, with $\delta^{60}\text{Ni}_M$ from -0.42 to -0.79‰ . MANOP $\delta^{60}\text{Ni}$ values are much
253 more negative than deep seawater, with $\delta^{60}\text{Ni}_{\text{seawater}} = +1.34 \pm 0.07\text{‰}$ (1 SD, seawater
254 samples $>200\text{m}$; Cameron and Vance, 2014; Takano et al., 2017; Wang et al., 2018;
255 Archer et al., 2020), and than Fe-Mn crusts, with $\delta^{60}\text{Ni}_{\text{FeMnCrust}} = +1.62 \pm 0.37\text{‰}$ (1
256 SD, Gall et al., 2013; Gueguen et al., 2016).

257



258

259 **Figure 4.** Ni isotope compositions for samples from MANOP site H (filled symbols)
260 and site M (open symbols) with depth in the sediment. Error bars (similar to symbol
261 size) are the long-term reproducibility of the secondary standard ($\pm 0.07\text{‰}$). Blue
262 dashed line: deep seawater $\delta^{60}\text{Ni}$ (Cameron and Vance, 2014; Takano et al., 2017;
263 Wang et al., 2018; Archer et al., 2020). Orange solid bar and shaded region: Fe-Mn
264 crust $\delta^{60}\text{Ni}$, mean and 1SD (Gall et al., 2013; Gueguen et al., 2016).

265

266 The Pacific Mn nodules from the ocean floor (Nod P1, 21KG-1n), which are
267 predominantly phyllomanganates, have $\delta^{60}\text{Ni}$ values of +0.34 and +0.28‰ (Table 2).

268 The two deeply buried nodules (22KL 530cm and 801cm), comprised mostly of
269 todorokite, have lower $\delta^{60}\text{Ni}$ values, at -0.08‰ and +0.01‰. The Peru Basin nodule
270 (77BC11-6) is also predominantly todorokite and is isotopically the lightest of the six
271 nodules, at -0.22‰. Nod A1 from the Atlantic has a heavier Ni isotope composition,
272 at $\delta^{60}\text{Ni} = +1.06\text{‰}$ (Table 2).

273

274 **5. Discussion**

275

276 The sediment samples from the two MANOP sites have the lightest Ni isotope
277 composition yet measured for modern marine sediments (at -0.2 to -0.8‰),
278 considerably lighter than Fe-Mn crusts (about +1.6‰; Gall et al., 2013; Gueguen et
279 al., 2016), organic-rich sediments (about +1.1‰; Ciscato et al., 2018), euxinic
280 sediments from the Black Sea (about +0.2‰; Vance et al., 2016), and the lithogenic Ni
281 isotope composition (about +0.1‰; Cameron et al., 2009). All MANOP samples are
282 also at least 20-fold enriched in Ni compared to the UCC (Fig. 3; Table 2); hence, the
283 lithogenic Ni component in these sediments is minor. We consider two possible
284 origins for isotopically light authigenic Ni: (1) an isotopically light source of Ni or (2)
285 isotope fractionation during diagenesis.

286

287 **5.1 An isotopically light source of Ni to the MANOP sites?**

288

289 One possible source of Ni to sediments is from the dissolved pool in seawater; a
290 diffusive flux of Ni was recently suggested to contribute to Ni accumulation in

291 oxygen-deficient continental margin sediments (Ciscato et al., 2018). However, a
292 diffusive flux requires higher Ni concentrations in bottom waters compared to
293 porewaters. Dissolved Ni concentrations measured in core-top porewaters at the
294 MANOP sites are similar to or, at site M, higher than bottom waters (Fig. 3;
295 Klinkhammer, 1980; Heggie et al., 1986), suggesting, if anything, a small benthic flux
296 of Ni *out* of porewaters. Alternatively, Ni in seawater may be scavenged by particulate
297 material in the water column, providing a ‘hydrogenetic’ source of Ni to sediments.
298 Models of hydrogenetic Fe-Mn crust formation have emphasized the importance of
299 inorganic sorption processes of this type (e.g., Koschinsky and Hein, 2003). If Fe-Mn
300 crusts represent the hydrogenetic Ni source to sediments, Ni that is isotopically similar
301 to or heavier than seawater, at $+1.62 \pm 0.37\%$ (1 SD, Gall et al., 2013; Gueguen et al.,
302 2016) would be expected in the MANOP sediments.

303

304 Nickel displays a typical nutrient-type profile in seawater (e.g., Bruland, 1980).
305 Furthermore, a strong correlation with organic carbon is observed in sediments
306 underlying upwelling zones, suggesting organic matter is an important supply route of
307 Ni to sediments (e.g., Fig S7; Ciscato et al., 2018). Cellular Ni/P ratios from the mixed
308 layer of the equatorial Pacific range from 0.25 – 1.15 mmol/mol (measured by
309 synchrotron XRF; Twining et al., 2012), similar to ratios for plankton tows from
310 nearby MANOP sites (0.51 to 0.96 mmol/mol; Collier and Edmond, 1984). Both
311 MANOP sites receive high fluxes of biogenic particulate material, with C_{org} rain rates
312 of 110 – 130 $\mu\text{g } C_{org}/\text{cm}^2/\text{yr}$ (Lyle et al., 1984). Given these values, we calculate that
313 approximately 5 – 10% of the Ni budget in the MANOP sediments is supplied by
314 organic matter (see Table S3 for details). However, higher particulate Ni/P ratios of
315 about 5 – 15 mmol/mol are observed below the mixed layer in the eastern Pacific (Fig.

316 S5; Ohnemus et al., 2017), suggesting that preferential P remineralisation occurs as
317 organic-rich particles settle through the water column (recently suggested in the
318 context of Cd/P; Bourne et al., 2018). The links between export production and
319 sedimentary metal concentrations is an area of active research, but we note that a
320 particulate Ni/P ratio of ~15 mmol/mol could account for ~100% of the Ni in the
321 MANOP sediments (Table S3).

322

323 Organic matter is therefore a significant source of Ni to the MANOP sediments, but is
324 it isotopically light? The limited dataset for upper water column $\delta^{60}\text{Ni}$ (Takano et al.,
325 2017; Wang et al., 2018; Archer et al., 2020) suggest that phytoplankton do
326 preferentially take up isotopically light Ni. However, the maximum fractionation
327 factor implied by water column data for biological uptake is rather small, at about –
328 0.3‰ (Archer et al., 2020). Consistent with this inference, Takano et al. (2020)
329 estimate the $\delta^{60}\text{Ni}$ of biogenic particles in the South China Sea to be +0.6 to +1‰.
330 Hence, Ni in organic matter exported from the photic zone is not expected to be nearly
331 light enough to explain the MANOP $\delta^{60}\text{Ni}$ values (at –0.2 to –0.8‰). Furthermore,
332 modern organic-rich sediments from the Peru margin have bulk Ni isotope
333 compositions of $+1.12 \pm 0.08\text{‰}$ (1SD, $n = 25$; Ciscato et al., 2018), consistent with the
334 water column data and suggesting that particle cycling on transit from the photic zone
335 to sediment is not associated with significant isotopic fractionation. Organic matter
336 cannot explain the light Ni isotope compositions observed at the MANOP sites.

337

338 A third possible source of Ni, particularly site M, which is 25 km east of the East
339 Pacific Rise, is hydrothermal sedimentation. To our knowledge, $\delta^{60}\text{Ni}$ values have not
340 been measured in hydrothermal fluids, but may be expected to be isotopically light,

341 similar to lithogenic Ni, at about +0.1‰ (Cameron et al., 2009). However, a direct Ni
342 source from hydrothermal fluids is unlikely; recent GEOTRACES sections suggest
343 that hydrothermal plumes may instead be sites of Ni removal from seawater via
344 scavenging (discussed by Ciscato et al., 2018). Using an endmember mixing model,
345 Fischer (1983) estimates that ~10% of the Ni (but ~50% of the Fe) at site M
346 (compared to <1% of the Ni at site H) is hydrothermally sourced. We consider a
347 possible role for hydrothermally sourced Fe to sedimentary Ni cycling at site M in
348 section 5.3.

349

350 **5.2 Nickel isotope fractionation during diagenesis: coupling of Ni-Mn**

351

352 Having ruled out an isotopically light source of Ni to the sediment, we suggest that
353 post-depositional processes are responsible for the MANOP Ni isotope compositions.
354 First, we consider two processes coupled to Mn diagenesis: (1) cycles of Mn oxide
355 dissolution and reprecipitation ('Mn cycling') and (2) transformation of birnessite to
356 todorokite ('todorokite transformation').

357

358 *Manganese cycling*

359 Porewater data from the MANOP sites (Klinkhammer, 1980; Heggie et al., 1986)
360 illustrate the clear coupling between Mn and Ni cycling – via cycles of Mn-oxide
361 dissolution and precipitation (Fig. 3). Sorbed Ni is released to porewaters upon Mn
362 oxide dissolution, and resorbed on newly precipitating Mn oxide phases within the
363 shallower oxygenated zone. Manganese oxides are strong sorbents for divalent trace
364 metals like Ni due to their negative surface layer charge at the pH of natural waters
365 (e.g., Burns and Burns, 1979; Koschinsky and Halbach, 1995). In particular,

366 phyllomanganates like birnessite, which has a layered structure of edge-sharing MnO_6
367 octahedra, are ubiquitous in the natural environment and are the main Mn-bearing and
368 trace metal-sorbing phases in oxic marine sediments (e.g., Peacock and Sherman,
369 2007a; Little et al., 2014). Experimental estimates of the magnitude of Ni isotope
370 fractionation on sorption to birnessite suggest a large light isotope effect, with a recent
371 study reporting $\Delta^{60}\text{Ni}_{\text{MnO}_2\text{-aqueous}} = -2.8$ to -3.4‰ (Sorensen et al., 2020).

372

373 The pattern of variation in Ni concentration and isotopic composition across the Black
374 Sea redoxcline (Vance et al., 2016) is qualitatively and quantitatively consistent with
375 these experimental data, with sorption to particulate Mn oxides above the redoxcline
376 preferring the light Ni isotopes by about 4%. We hypothesize that a similar process
377 takes place in sediment porewaters, explaining (at least in part) the light isotopic
378 compositions of the MANOP sediments. The smaller $\Delta^{60}\text{Ni}_{\text{MANOP-seawater}}$ offset of
379 about -1.6 to -2.4‰ compared to experiments and the Black Sea likely reflects the
380 fact that the porewater-sediment system is not completely open.

381

382 In the context of the experimental data, the observations in the Black Sea, and the new
383 data here, the published data for hydrogenetic Fe-Mn crusts stand out as different.
384 Most Fe-Mn crusts analysed to date are isotopically similar to or heavier than seawater
385 (Fig. 5A). Sorensen et al. (2020) suggest three possible explanations for this
386 observation. The first involves differences in the mechanism of incorporation into the
387 solid structure. Nickel in slow-growing Fe-Mn crusts is predominantly structurally
388 incorporated into birnessite (specifically vernadite/ $\delta\text{-MnO}_2$) vacancy sites (Peacock
389 and Sherman, 2007a), while adsorption in experiments occurs primarily as a triple-
390 corner-sharing surface complex over the vacancy sites (Peacock and Sherman, 2007b;

391 Sorensen et al., 2020). Surface complexation is also likely to be dominant in dynamic
392 open system environments like the redoxcline of the Black Sea. It is possible,
393 therefore, that structural incorporation of Ni is associated with a different isotope
394 effect than adsorption as a surface complex. A second explanation relates to reaction
395 kinetics, with slow-growing (a few mm/Ma) Fe-Mn crusts exhibiting long-term
396 isotopic equilibration of Ni with seawater; exchangeability of Ni in Fe-Mn crusts has
397 recently been demonstrated by Hens et al. (2019). Finally, it has been suggested that
398 Ni speciation in seawater may control the isotopic composition of the sorbing Ni
399 species, with a possible role for organic complexation (Sorensen et al., 2020).

400

401 Fe-Mn crusts are not only marked by relatively positive $\delta^{60}\text{Ni}$ values, but also by
402 significant variability in $\delta^{60}\text{Ni}$ (Fig. 5A, +0.41 to +2.47‰; Gall et al., 2013), which
403 may reflect the complexities of the aforementioned processes. We note, however, that
404 a depth profile through one crust (ZEP2-DR05-04) from the Pacific Ocean shows a
405 marked transition towards much lighter Ni isotope compositions coupled to decreasing
406 Mn/Ni ratios at depth (Fig. 5B; Gueguen et al., 2016). The authors attributed this
407 transition to lighter isotopic compositions to the reductive dissolution of primary Mn
408 oxide phases followed by their reprecipitation and the resorption of Ni in an open
409 system (Gueguen et al., 2016) – i.e. the same process of Mn cycling described here.

410

411 Phylломanganate-rich surface Mn nodules may also record the impact of Mn cycling
412 in their Ni isotope compositions, because they contain Ni from both hydrogenetic and
413 diagenetic sources. They consist of hydrogenetic layers formed by precipitation from
414 seawater (vernadite/ δ -MnO₂ and amorphous FeOOH) and diagenetic layers formed
415 during re-precipitation from sub-oxic porewaters (primarily 7 and 10 Å birnessite)

416 (e.g., Koschinsky and Halbach, 1995; Heller et al., 2018). These nodules are variably
417 isotopically light (at +0.28 to +1.06‰) compared to seawater, and fall close to the
418 Mn/Ni v $\delta^{60}\text{Ni}$ evolution line of the Fe-Mn crust affected by Mn cycling (Fig. 5B,
419 Gueguen et al., 2016).

420

421 Overall, a consistent picture of the impact of Mn cycling on Ni isotope compositions
422 emerges from the MANOP sediments, Fe-Mn crusts and Mn nodules. Hydrogenetic
423 $\delta^{60}\text{Ni}$ values (represented by Fe-Mn crusts) are similar to the seawater Ni isotope
424 composition, with Mn cycling during diagenesis leading to partial dissolution and
425 reprecipitation of phyllomanganates that re-scavenge isotopically light Ni in a variably
426 open system, associated with decreasing Mn/Ni ratios.

427

428 *Todorokite transformation*

429 During diagenesis, birnessite can also transform (via a 10 Å phase) to the
430 tectomanganate todorokite (Atkins et al., 2014; Wegorzewski et al., 2020). Recent
431 experimental work suggests that this transformation leads to significant Ni release to
432 porewaters, because Ni is not significantly incorporated in the todorokite crystal
433 structure (Atkins et al., 2016). Consistent with this finding, buried Mn nodules of
434 todorokite exhibit *higher* Mn/Ni ratios compared to phyllomanganate-rich surface
435 nodules (Fig. 5B; Heller et al., 2018; Wegorzewski et al., 2020), i.e. the opposite
436 evolution to that inferred for Mn cycling. Furthermore, buried nodules are isotopically
437 even lighter (at -0.22 to +0.01‰) than surface nodules (at +0.28 to +1.06‰),
438 suggesting that todorokite transformation may lead to further Ni isotope fractionation.

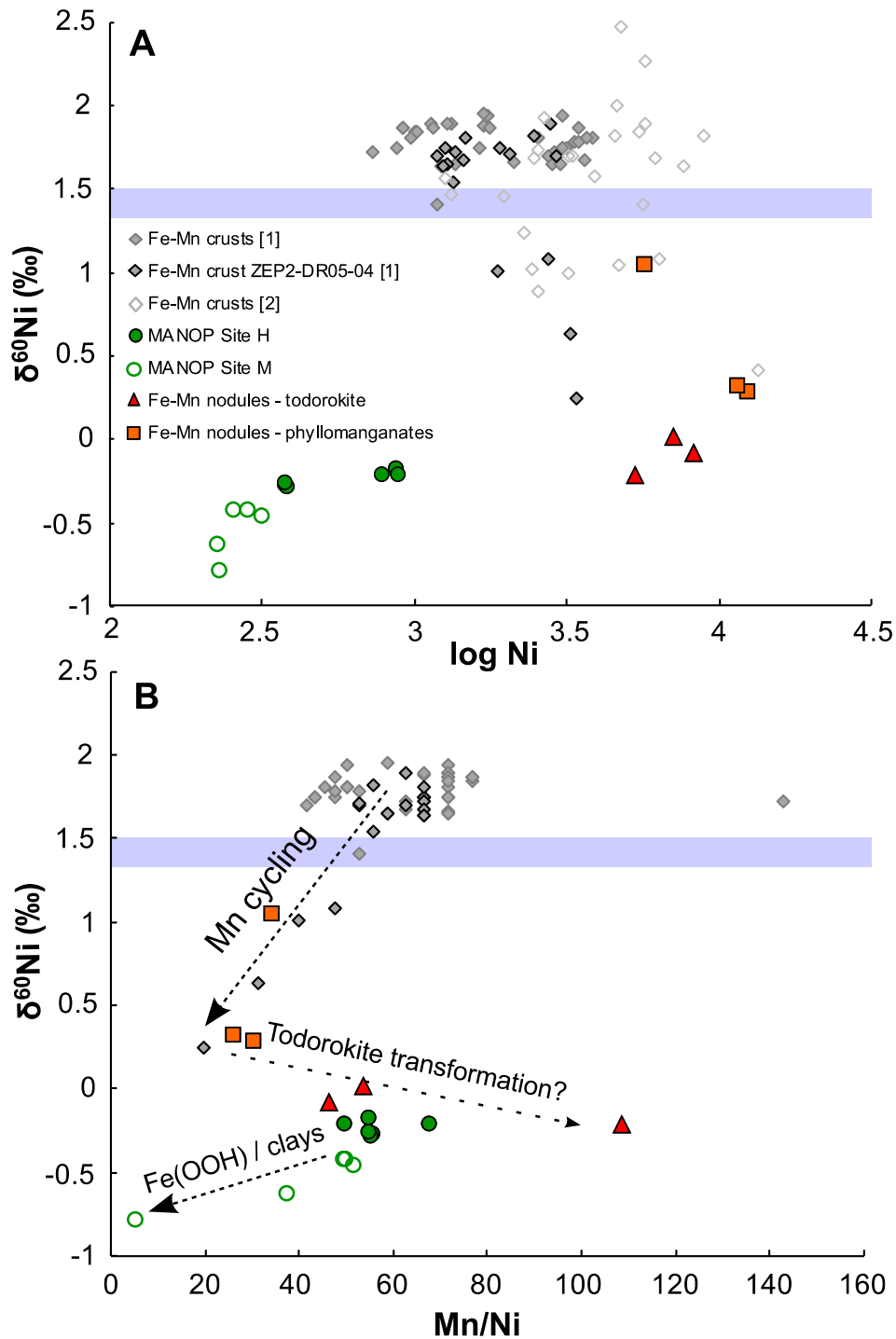
439

440 However, the relevance of todorokite transformation to the Ni isotope composition of
441 the MANOP sediments, and to marine Ni cycling more broadly, remains unclear,
442 because the timescale and mechanism of todorokite transformation and its prevalence
443 in marine sediments is difficult to establish. Typically considered a process of
444 phylломanganate ageing under oxic conditions, oxic transformation of birnessite to
445 todorokite in the lab has only been achieved at higher than ambient temperatures
446 and/or lower than circumneutral pH (e.g., Atkins et al., 2014). Recently, Jung et al.
447 (2020) demonstrate that cyclic redox fluctuations (driven in the lab by cyclic
448 voltammetry) can also trigger the layer-to-tunnel phase transformation. Cyclic redox
449 fluctuations are common in marine sediments, suggesting that todorokite
450 transformation may occur outside of fully oxic diagenetic settings. Nevertheless,
451 identification of todorokite by XRD is currently impossible at the low abundances
452 present in marine sediments, due to the similar crystallographic structure of different
453 Mn oxide polymorphs. While our XRD data for the MANOP sediments indicates the
454 presence of a phylломanganate phase, we cannot rule out the occurrence of more
455 crystalline todorokite at low abundance. Geochemically, MANOP Mn/Ni ratios are
456 more similar to those of the buried, todorokite-rich Mn nodules than to surface
457 nodules, but they are also similar to hydrogenetic Pacific Fe-Mn crusts (Fig. 5B).

458

459 Future experimental work will test the hypothesis that todorokite transformation leads
460 to preferential retention of isotopically light Ni in the solid phase, and investigate the
461 relationships between the transformation mechanism, Ni release, and evolving Mn/Ni
462 ratios.

463



464

465 **Figure 5.** A) log Ni concentration and B) Mn/Ni ratios versus $\delta^{60}\text{Ni}$ values for samples
 466 from MANOP site H (green filled circles), MANOP site M (green open circles), Mn
 467 nodules of predominantly phyllomanganates (orange squares) and todorokite (red
 468 triangles), and literature values for Fe-Mn crusts (grey diamonds). Labelled dashed
 469 arrows in B represent the proposed diagenetic effects of Mn cycling, todorokite
 470 transformation, and scavenging by Fe (hydr)oxides or authigenic clays (see text for
 471 details). Error bars on $\delta^{60}\text{Ni}$ values are approximately the size of the symbols (\pm
 472 0.07‰). Literature data: [1] Gueguen et al. (2016) and [2] Gall et al. (2013) (Note: No
 473 Mn data are presented by Gall et al., 2013).

474 **5.3 Nickel isotope fractionation during diagenesis: Fe (hydr)oxides or authigenic**
475 **clays?**

476

477 We suggest that the diagenetic cycling of Ni coupled to Mn is the key control on the
478 Ni isotope compositions of the MANOP sediments. However, the sample with the
479 lightest Ni isotope composition (at -0.79%), from 18 cm depth at site M, has the
480 lowest Mn concentration (0.12 wt%) and lowest Mn/Ni ratio (5.4, Fig. 5B). Despite
481 limited Mn enrichment, this sample is significantly Ni enriched ($\text{Ni}/\text{Al} = 0.0056$ cf.
482 $\text{Ni}/\text{Al}_{\text{UCC}} = 0.0006$). Together, these observations suggest an additional control on Ni
483 isotope compositions in low Mn sediments. We consider two possibilities: (1) sorption
484 of isotopically light Ni on nanoscale Fe (hydr)oxides, and (2) incorporation of
485 isotopically light Ni in Fe-rich authigenic clays.

486

487 *Nanoscale Fe oxides*

488 Iron is significantly more enriched at site M ($\text{Fe}/\text{Al} \sim 1.3$) compared to site H (Fe/Al
489 ~ 0.8 ; Fig. 3), with the difference attributed to the presence of hydrothermal
490 precipitates at site M (Fischer, 1983). Sorption of Ni on Fe (hydr)oxides is less
491 energetically favoured than on phyllophanates, due to the higher pH_{pzc} for Fe
492 (hydr)oxide phases (at about 7 to 8) compared to MnO_2 (at about 2, Stumm and
493 Morgan, 1996; Tripathy and Kanungo, 2005). Nevertheless, when phyllophanates
494 are scarce, Fe (hydr)oxide phases become environmentally relevant.

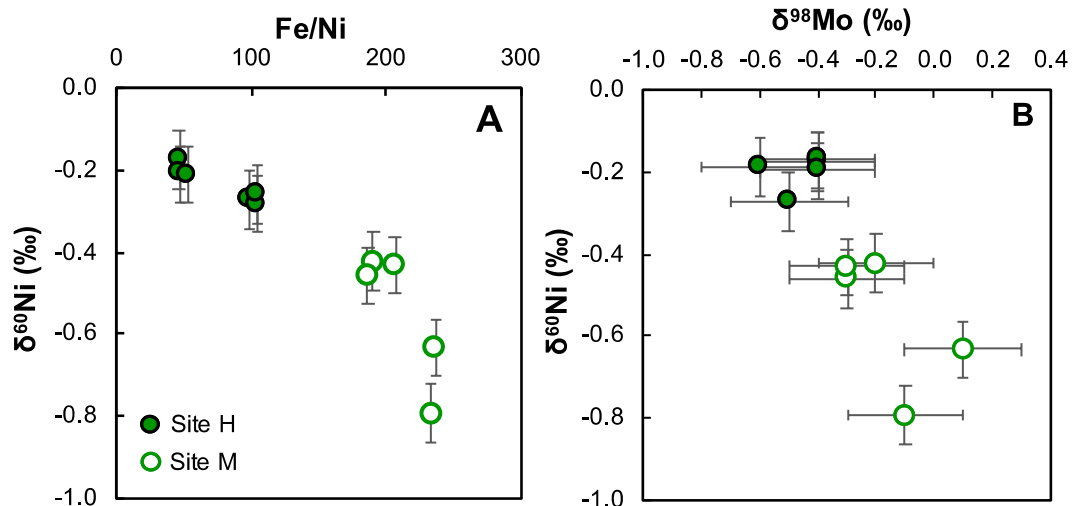
495

496 Experimental investigations of Ni isotope fractionation on sorption to ferrihydrite
497 found $\Delta^{60}\text{Ni}_{\text{ferrihydrite-aqueous}} = -0.35\%$ (Wasylenki et al., 2015; Gueguen et al., 2018).
498 For Ni coprecipitation with ferrihydrite, Wang and Wasylenki (2017) found that the

499 fractionation factor increased from -0.08 to -0.50‰ with increased co-precipitation
500 (e.g., at higher pH). Sorption to goethite is associated with a larger fractionation factor,
501 $\Delta^{60}\text{Ni}_{\text{goethite-aqueous}} = -0.77\text{‰}$ (Gueguen et al., 2018). A correlation is observed between
502 Fe/Ni and Ni isotope compositions at site M (Fig. 6A), consistent with the hypothesis
503 of scavenging of isotopically light Ni by Fe (hydr)oxide phases. We envisage that this
504 process occurs during diagenesis, due to the evolution towards lighter Ni isotope
505 compositions at site M compared to site H. (Fig. 6A) However, it is also feasible that
506 dissolved Ni is scavenged by hydrothermal Fe precipitates suspended in the water
507 column and which subsequently settle out.

508

509 Interestingly, $\delta^{60}\text{Ni}$ also correlates with published $\delta^{98}\text{Mo}$ values for the MANOP
510 samples (Fig 6B; Poulson Brucker et al., 2009). Like Ni, Mo cycling has been strongly
511 linked to Mn in oxic marine sediments, but a role for sorption to Fe (hydr)oxides in the
512 oceanic Mo cycle has also been proposed (Goldberg et al., 2009). Molybdenum
513 sorption on Mn oxides exhibits a stronger preference for light isotopes (e.g., Barling
514 and Anbar, 2004) than Mo sorption on Fe (hydr)oxides (Goldberg et al., 2009). Thus,
515 these two competing controls on Mo isotope compositions appear to be consistent with
516 the MANOP $\delta^{98}\text{Mo}$ values, in which the site M samples (rich in Fe) are isotopically
517 heavier than those of site H (rich in Mn).



518

519 **Figure 6.** Relationships between A. Fe/Ni and B. $\delta^{98}\text{Mo}$ (data: Poulson Brucker et al.,
 520 2009) and Ni isotope compositions at the two MANOP sites. Error bars on $\delta^{60}\text{Ni}$ are
 521 the long-term reproducibility ($\pm 0.07\text{‰}$) and on $\delta^{98}\text{Mo}$ are $\pm 0.20\text{‰}$ (the estimated
 522 external reproducibility on bulk $\delta^{98}\text{Mo}$ values from Poulson Brucker et al., 2009).
 523

524 *Authigenic clay minerals*

525 Though it has long been inferred that authigenic Fe (hydr)oxide coatings are an
 526 important host phase for trace elements in marine sediments, direct image-based
 527 identification of these phases has proven challenging. The XRD technique utilised in
 528 this study, for example, has a detection limit of ~ 2 wt% for Fe (hydr)oxide phases.
 529 However, it has been suggested that part of the challenge in directly observing Fe
 530 (hydr)oxide coatings reflects the fact that authigenic Fe is (at least partly) hosted in
 531 authigenic clay minerals (e.g., Abbott et al., 2019). By extension, it is possible that Fe
 532 (hydr)oxides are not as quantitatively important scavengers of trace elements, and that
 533 authigenic clay minerals play an under-appreciated role (e.g., Hein et al., 1979; Abbott
 534 et al., 2019).

535

536 The dominant mineral phase at both MANOP sites is smectite; indeed, authigenic
 537 smectite (Fe-rich montmorillonite) makes up 26 to 66% of the clays present in north
 538 equatorial Pacific sediments (Hein et al., 1979). Hein et al. (1979) found that this

539 smectite contains 70 – 150 $\mu\text{g/g}$ Ni, though the clay fraction analysed may have
540 included sorbed nanoscale Fe (hydr)oxides. Nevertheless, using x-ray absorption
541 spectroscopy, Merrot et al. (2019) find that Ni is primarily hosted by Fe-rich smectite
542 and early diagenetic greenalite in lagoon sediments. During terrestrial weathering, Ni
543 liberated from primary minerals is concentrated by smectite, where present (e.g., Ratié
544 et al., 2018). Furthermore, the smectitic zone of a weathering profile is characterized
545 by light Ni isotope compositions compared to the protolith (Ratié et al., 2018),
546 consistent with experimental results indicating a small light isotope effect on sorption
547 to Na-montmorillonite (a form of smectite), of $-0.11 \pm 0.09\text{‰}$ (Spivak-Birndorf et al.,
548 2018). We suggest that better evaluation of the role of authigenic clays in sedimentary
549 trace element budgets should be a target for future research.

550

551

552 **5.4 Implications for whole oceanic mass balance**

553

554 Assuming steady state, there is a significant flux and isotopic mass imbalance in the
555 oceanic Ni cycle, summarised most recently by Ciscato et al. (2018). In their analysis,
556 the input of Ni (riverine dissolved Ni and Ni from mineral dust) is 3.7×10^8 mol/year,
557 with $\delta^{60}\text{Ni}_{\text{input}} = +0.79\text{‰}$. By contrast, the estimated output flux to sediments ranges
558 from 7.2 to 17×10^8 mol/year (i.e. 2–5 times larger than the estimated input flux), with
559 $\delta^{60}\text{Ni}_{\text{output}} \approx +1.5\text{‰}$. By far the dominant feature of the existing Ni budget is the
560 removal flux to dispersed Fe-Mn oxides in ‘oxic sediments’ (where oxygen penetrates
561 to >1 cm depth; Morford and Emerson, 1999), which is estimated to range from 5.8 to
562 10.5×10^8 mol/yr (Gall et al., 2013; Cameron and Vance, 2014). The isotopic

563 composition of this oxic sink has been assumed to reflect that of Fe-Mn crusts, at
564 about +1.6‰.

565

566 Ciscato et al. (2018) suggest that the previously assumed flux of Ni to the oxic sink,
567 and its isotopic composition, might be erroneous. Balancing the budget would require
568 an oxic sink of 1.8×10^8 mol/yr (3–5 times smaller than previously estimated), with an
569 average isotopic composition of about +0.5‰. Our study suggests a resolution of this
570 problem, via the diagenetic remobilization of isotopically heavy Ni and its release into
571 bottom waters. From here on, we assume that this diagenetic remobilization and
572 release occurs in sub-oxic (specifically, Mn reducing) settings. However, we note that
573 todorokite transformation may also occur in oxic settings, and thus this process may be
574 significantly underrepresented in the following assessment.

575

576 First, we recalculate the Ni burial flux in oxic sediments by coupling to estimates for
577 Mn. The authigenic accumulation rate of Mn in pelagic clays is estimated at 6 – 23
578 $\mu\text{mol}/\text{cm}^2/\text{kyr}$ (best guess: $13 \mu\text{mol}/\text{cm}^2/\text{kyr}$) (Rehkämper and Nielsen, 2004 and
579 references therein). The Ni/Mn ratio of the MANOP site H sediments and of Fe-Mn
580 crusts is 0.019 (by weight; USGS compilation of Manheim and Lane-Bostwick, 1991).
581 Of the sediment types described in the marine sediment census of Dutkiewicz et al.
582 (2015), we include only ‘clay’ (40.2% ocean area) in this category. The remainder are
583 predominantly calcareous oozes, which have a low Mn content (Morford and
584 Emerson, 1999 and references therein), though we note that two ‘transitional’
585 sediment types (‘siliceous mud’, 5.0% and ‘fine-grained calcareous sediment’, 12.4%;
586 Dutkiewicz et al., 2015) may be a significant Mn sink and should be a target of future
587 studies. We estimate a Ni burial flux to oxic sediments (in this case, exclusively clay)

588 of 1.5 to 5.9×10^8 mol/yr (Table 3). Nickel burial in association with carbonates is
589 negligible on this scale, at about 0.14×10^8 mol/year (Ciscato et al., 2018). Following
590 previous authors, we assume that the Ni isotope composition of oxic sediments is
591 represented by Fe-Mn crusts, at $+1.62 \pm 0.37\text{‰}$ (1 SD, Table 3; Gall et al., 2013;
592 Gueguen et al., 2016).

593

594 Next, we estimate the benthic return flux of Ni *from* sub-oxic sediments, also by
595 comparison to Mn. Morford and Emerson (1999) estimate that sub-oxic sediments
596 (defined as those deposited at >1000 m water depth for which oxygen penetrates to ≤ 1
597 cm) cover $\sim 4\%$ of the ocean area. They estimate a sub-oxic benthic Mn flux of $0.7 -$
598 1.3×10^{10} mol/yr (Morford and Emerson, 1999). Our study suggests that Mn
599 diagenesis leads to preferential retention of Ni in sediments compared to Mn (Fig. 5B),
600 but todorokite transformation should have the opposite effect (Fig. 5B; Atkins et al.,
601 2016). Direct measurements of porewater Ni/Mn ratios for the MANOP sediments are
602 variable, but generally similar to the solid phase (i.e. ~ 0.019) ranging from $0.005 -$
603 0.031 (mean site M = 0.009 , mean site H = 0.020 ; Klinkhammer, 1980). For an
604 estimated Ni/Mn range of $0.009 - 0.020$, we calculate a benthic Ni flux of $0.6 - 2.3 \times$
605 10^8 mol/yr.

606

607 Next, we solve for the isotopic composition of the benthic flux by expanding equation
608 (1) for all known fluxes and assuming steady state, where:

609

$$610 \quad (3) \quad F_{\text{river}}\delta_{\text{river}} + F_{\text{dust}}\delta_{\text{dust}} + F_{\text{benthic}}\delta_{\text{benthic}} = F_{\text{oxic}}\delta_{\text{oxic}} + F_{\text{org}}\delta_{\text{org}} + F_{\text{eux}}\delta_{\text{eux}} + F_{\text{carb}}\delta_{\text{carb}}$$

611

612 In equation (3), the Ni sources include rivers, dust and the benthic flux, while the sinks
613 are pelagic clays ('oxic'), organic-rich sediments on continental margins ('org'),
614 euxinic sediments ('eux') and carbonates ('carb').

615

616 We carry out a Monte Carlo simulation (10,000 iterations), allowing each flux to vary
617 within its given range (flux and $\delta^{60}\text{Ni}$; values given in italics in Table 3) and solving
618 for the benthic flux required to balance the Ni mass budget (model results in bold in
619 Table 3). Flux magnitudes were forced by uniformly distributed random numbers, and
620 isotopic compositions by normally distributed random numbers (around the mean and
621 standard deviation of published data, see Table 3). For further discussion of the
622 approach, see the Supplementary Information. Note that the carbonate and euxinic
623 sinks, and the dust source, are minor, and therefore represented in the simulation
624 simply by the best guess at their magnitudes and isotopic compositions (Table 3). The
625 riverine flux is included as the concentration and discharge-weighted average of
626 Cameron and Vance (2014). Post-simulation, the benthic flux range was restricted to
627 $0.6 - 2.3 \times 10^8$ mol/yr, with the side effect of reducing the maximum output flux to
628 pelagic clays to 4.6×10^8 mol/yr (see SI for further discussion).

629

630 This analysis suggests that the isotopic composition of the benthic flux required to
631 balance the oceanic Ni budget is approximately +3‰ (Table 3). Compared to the
632 isotopic composition of oxic sediments (at +1.6‰), this equates to an effective
633 fractionation factor for diagenesis of about -1.4‰ (averaged globally). This value is
634 comparable to the observed isotopic difference between the MANOP sediments (at
635 about -0.2 to -0.8‰) and the possible sources of Ni to the site (at about +0.1 to

636 +1.6‰; Section 5.1), supporting the hypothesis that diagenetic remobilisation of
637 isotopically heavy Ni can balance the oceanic Ni budget.

638

639

640 **Table 3.** Modelled oceanic mass balance of Ni and Ni isotopes (see text and SI for full
641 details). Values in italics were used in the Monte Carlo simulation. Values in bold are
642 outputs from the model.

	Flux ($\times 10^8$ mol/yr)		$\delta^{60}\text{Ni}$ (‰)	
	Range	Best guess	Mean and SD or range	Best guess or range
<u>Source fluxes</u>				
Rivers ^a	-	<i>3.60</i>	-	<i>0.8</i>
Dust ^{b,c}	-	<i>0.076</i>	-0.09 to 0.37	<i>0.14</i>
Benthic	<i>0.6 to 2.3</i>	1.44	3.17 \pm 1.08	3.03*
<u>Sink fluxes</u>				
Pelagic clays	<i>1.5 to 4.6 (5.9)</i>	3.08	<i>1.62 \pm 0.37^d</i>	<i>1.62</i>
Organic-rich ^b	<i>1.1 to 2.4</i>	1.74	<i>1.12 \pm 0.08</i>	<i>1.12</i>
Carbonates ^b	0.031 to 0.44	<i>0.14</i>	1.10 to 1.64	<i>1.29</i>
Euxinic ^b	0.093 to 0.25	<i>0.15</i>	0.3 to 0.6 ^c	<i>0.45</i>
Total in/out	4.3 to 6.0	5.1	1.41 \pm 0.23	1.40
Residence time ¹	18 to 25 kyr	21 kyr		

643 *Best guess $\delta^{60}\text{Ni}$ is the median value output by the model (For details see SI, Fig. S8).

644 ¹Residence time calculated given a global ocean volume of 1.35×10^{21} kg and mean
645 Ni concentration of 8 nM (i.e. 1.08×10^{13} moles Ni).

646 References: ^aCameron and Vance (2014), ^bCiscato et al. (2018), ^cVance et al. (2016),
647 ^dGall et al. (2013).

648

649

650 **6. Conclusions**

651

652 We report Ni isotope compositions for metalliferous sediments from two of the eastern
653 Pacific MANOP sites. Both sites exhibit very light Ni isotope compositions (at -0.8 to
654 -0.2‰) compared to hydrogenetic Fe-Mn crusts (at +1.6‰). Low but variable $\delta^{60}\text{Ni}$
655 values are also observed for Mn nodules (-0.2 to +1.0‰). We propose two primary
656 mechanisms to explain the isotopically light diagenetic Ni ‘fingerprint’: (1) Mn
657 cycling, in which Ni cycling is coupled to the redox-driven dissolution and
658 reprecipitation of Mn oxides, and (2) the mineralogical transformation of birnessite to
659 todorokite, which may occur in oxic or sub-oxic sedimentary environments. In Mn-
660 poor oxic sediments we suggest that additional Ni (and Mo) isotope fractionation

661 accompanies the scavenging of isotopically light Ni by nanoscale Fe (hydr)oxides or
662 Fe-rich authigenic clays.

663

664 We hypothesize that diagenetic remobilization of isotopically heavy Ni balances the
665 oceanic Ni budget. Based on estimates for Mn, we calculate a benthic Ni flux of 0.6 to
666 2.3×10^8 mol/yr, comparable in magnitude to the riverine Ni flux, at 3.6×10^8 mol/yr.
667 The required isotopic composition of this benthic flux to balance the oceanic Ni
668 budget is approximately +3‰, providing a testable hypothesis for future studies. Our
669 calculation does not directly consider the under-constrained possibility of Ni release
670 during the transformation of phyllosulfates to todorokite in oxic marine sediments,
671 a process that would not be associated with a benthic Mn flux. Further lab and field-
672 based investigations are underway targeting the analysis of oxic and sub-oxic
673 sediments and porewaters, and to investigate the Ni isotope fractionation associated
674 with todorokite transformation.

675

676 **Acknowledgements**

677 We would like to thank Francis Albarède and an anonymous reviewer for their
678 comments on a previous version of this paper. SHL is supported by a NERC
679 independent research fellowship (NE/P018181/1). ETH involvement in this research
680 was supported by the Swiss National Science Foundation (SNF) through grants
681 200020-16590 and 200021_184873/1 (to DV). JM's contributions were supported by
682 NSF grant 1657832. The authors would like to thank Emily Ciscato and Aditi
683 Chatterjee for helpful discussions during the project, Rhian O'Callaghan for making
684 Figure 1, Caroline Peacock for feedback on an earlier version of the manuscript, and
685 Matthias Haeckel for providing the Peru Basin nodule sample (77BC11-6).

686

687

688 **References**

689

690 Abbott, A.N., Löhr, S., Trethewy, M., 2019. Are Clay Minerals the Primary Control
691 on the Oceanic Rare Earth Element Budget? *Front. Mar. Sci.* 6, 1–19.

692 <https://doi.org/10.3389/fmars.2019.00504>

693 Archer, C., Vance, D., Lohan, M.C., Milne, A., 2020. The oceanic biogeochemistry of
694 nickel and its isotopes: new data from the South Atlantic and the Southern Ocean
695 biogeochemical divide. *Earth Planet. Sci. Lett.*

696 Atkins, A.L., Shaw, S., Peacock, C.L., 2016. Release of Ni from birnessite during
697 transformation of birnessite to todorokite: Implications for Ni cycling in marine
698 sediments. *Geochim. Cosmochim. Acta* 189, 158–183.

699 <https://doi.org/10.1016/j.gca.2016.06.007>

700 Atkins, A.L., Shaw, S., Peacock, C.L., 2014. Nucleation and growth of todorokite
701 from birnessite: Implications for trace-metal cycling in marine sediments.

702 *Geochim. Cosmochim. Acta* 144, 109–125.

703 <https://doi.org/10.1016/j.gca.2014.08.014>

704 Barling, J., Anbar, A.D., 2004. Molybdenum isotope fractionation during adsorption
705 by manganese oxides. *Earth Planet. Sci. Lett.* 217, 315–329.

706 [https://doi.org/10.1016/S0012-821X\(03\)00608-3](https://doi.org/10.1016/S0012-821X(03)00608-3)

707 Bourne, H.L., Bishop, J.K.B., Lam, P.J., Ohnemus, D.C., 2018. Global Spatial and
708 Temporal Variation of Cd:P in Euphotic Zone Particulates. *Global Biogeochem.*
709 *Cycles.* <https://doi.org/10.1029/2017GB005842>

710 Bruland, K.W., 1980. Oceanographic distributions of cadmium, zinc, nickel and
711 copper in the North Pacific. *Earth Planet. Sci. Lett.* 47, 176–198.

712 Burns, R.G., Burns, V.M., 1979. Manganese oxides, in: Burns, R.G. (Ed.), *Marine*
713 *Minerals.* pp. 1–46.

714 Cameron, V., Vance, D., 2014. Heavy nickel isotope compositions in rivers and the
715 oceans. *Geochim. Cosmochim. Acta* 128, 195–211.

716 <https://doi.org/10.1016/j.gca.2013.12.007>

717 Cameron, V., Vance, D., Archer, C., House, C.H., 2009. A biomarker based on the
718 stable isotopes of nickel. *Proc. Natl. Acad. Sci.* 106, 10944–10948.

719 <https://doi.org/10.1073/pnas.0900726106>

720 Ciscato, E.R., Bontognali, T.R.R., Vance, D., 2018. Nickel and its isotopes in organic-
721 rich sediments: implications for oceanic budgets and a potential record of ancient
722 seawater. *Earth Planet. Sci. Lett.* 494, 239–250.
723 <https://doi.org/10.1016/j.epsl.2018.04.061>

724 Collier, R., Edmond, J., 1984. The trace element geochemistry of marine biogenic
725 particulate matter. *Prog. Oceanogr.* 13, 113–199. [https://doi.org/10.1016/0079-
726 6611\(84\)90008-9](https://doi.org/10.1016/0079-6611(84)90008-9)

727 Dutkiewicz, A., Müller, R.D., O’Callaghan, S., Jónasson, H., 2015. Census of seafloor
728 sediments in the world’s ocean. *Geology* 43, 795–798.
729 <https://doi.org/10.1130/G36883.1>

730 Fischer, K., 1983. Particle Fluxes in the Eastern Tropical Pacific Ocean - Sources and
731 Processes. Oregon State University.

732 Gall, L., Williams, H.M., Siebert, C., Halliday, A.N., Herrington, R.J., Hein, J.R.,
733 2013. Nickel isotopic compositions of ferromanganese crusts and the constancy
734 of deep ocean inputs and continental weathering effects over the Cenozoic. *Earth
735 Planet. Sci. Lett.* 375, 148–155. <https://doi.org/10.1016/j.epsl.2013.05.019>

736 Goldberg, T., Archer, C., Vance, D., Poulton, S.W., 2009. Mo isotope fractionation
737 during adsorption to Fe (oxyhydr)oxides. *Geochim. Cosmochim. Acta* 73, 6502–
738 6516. <https://doi.org/10.1016/j.gca.2009.08.004>

739 Gueguen, B., Rouxel, O., Rouget, M.L., Bollinger, C., Ponzevera, E., Germain, Y.,
740 Fouquet, Y., 2016. Comparative geochemistry of four ferromanganese crusts
741 from the Pacific Ocean and significance for the use of Ni isotopes as
742 paleoceanographic tracers. *Geochim. Cosmochim. Acta* 189, 214–235.
743 <https://doi.org/10.1016/j.gca.2016.06.005>

744 Gueguen, B., Sorensen, J. V., Lalonde, S. V., Peña, J., Toner, B.M., Rouxel, O., 2018.
745 Variable Ni isotope fractionation between Fe-oxyhydroxides and implications for
746 the use of Ni isotopes as geochemical tracers. *Chem. Geol.*
747 <https://doi.org/10.1016/j.chemgeo.2018.01.023>

748 Heggie, D., Kahn, D., Fischer, K., 1986. Trace metals in metalliferous sediments,
749 MANOP Site M: interfacial pore water profiles. *Earth Planet. Sci. Lett.* 80, 106–
750 116. [https://doi.org/10.1016/0012-821X\(86\)90023-3](https://doi.org/10.1016/0012-821X(86)90023-3)

751 Hein, J.R., Yeh, H.-W., Alexander, E., 1979. Origin of Iron-Rich Montmorillonite
752 from the Manganese Nodule Belt of the North Equatorial Pacific. *Clays Clay
753 Miner.* 27, 185–194. <https://doi.org/10.1346/ccmn.1979.0270303>

754 Heller, C., Kuhn, T., Versteegh, G.J.M., Wegorzewski, A. V., Kasten, S., 2018. The
755 geochemical behavior of metals during early diagenetic alteration of buried
756 manganese nodules. *Deep. Res. Part I Oceanogr. Res. Pap.* 142, 16–33.
757 <https://doi.org/10.1016/j.dsr.2018.09.008>

758 Hens, T., Brugger, J., Etschmann, B., Paterson, D., Brand, H.E.A., Whitworth, A.,
759 Frierdich, A.J., 2019. Nickel exchange between aqueous Ni(II) and deep-sea
760 ferromanganese nodules and crusts. *Chem. Geol.* 528, 119276.
761 <https://doi.org/10.1016/J.CHEMGEO.2019.119276>

762 Jaun, B., Thauer, R.K., 2007. Methyl-Coenzyme M Reductase and its Nickel Corphin
763 Coenzyme F430 in Methanogenic Archaea, in: *Nickel and Its Surprising Impact in*
764 *Nature.* <https://doi.org/10.1002/9780470028131.ch8>

765 Jung, H., Taillefert, M., Sun, J., Wang, Q., Borkiewicz, O.J., Liu, P., Yang, L., Chen,
766 S., Chen, H., Tang, Y., 2020. Redox Cycling Driven Transformation of Layered
767 Manganese Oxides to Tunnel Structures. *J. Am. Chem. Soc.*
768 <https://doi.org/10.1021/jacs.9b12266>

769 Kadko, D.C., 1981. A detailed study of uranium-series nuclides for several sediment
770 reimes of the Pacific. Columbia University.

771 Kessler, W.S., 2006. The circulation of the eastern tropical Pacific: A review. *Prog.*
772 *Oceanogr.* <https://doi.org/10.1016/j.pocean.2006.03.009>

773 Klinkhammer, G.P., 1980. Early diagenesis in sediments from the eastern equatorial
774 Pacific, II. Pore water metal results. *Earth Planet. Sci. Lett.* 49, 81–101.
775 [https://doi.org/10.1016/0012-821X\(80\)90151-X](https://doi.org/10.1016/0012-821X(80)90151-X)

776 Koschinsky, A., Halbach, P., 1995. Sequential leaching of marine ferromanganese
777 precipitates: Genetic implications. *Geochim. Cosmochim. Acta* 59, 5113–5132.
778 [https://doi.org/10.1016/0016-7037\(95\)00358-4](https://doi.org/10.1016/0016-7037(95)00358-4)

779 Koschinsky, A., Hein, J.R., 2003. Uptake of elements from seawater by
780 ferromanganese crusts: Solid-phase associations and seawater speciation. *Mar.*
781 *Geol.* 198, 331–351. [https://doi.org/10.1016/S0025-3227\(03\)00122-1](https://doi.org/10.1016/S0025-3227(03)00122-1)

782 Krishnaswami, S., 1976. Authigenic transition elements in Pacific pelagic clays.
783 *Geochim. Cosmochim. Acta* 40, 425–434. [https://doi.org/10.1016/0016-](https://doi.org/10.1016/0016-7037(76)90007-7)
784 [7037\(76\)90007-7](https://doi.org/10.1016/0016-7037(76)90007-7)

785 Little, S.H., Sherman, D.M., Vance, D., Hein, J.R., 2014. Molecular controls on Cu
786 and Zn isotopic fractionation in Fe-Mn crusts. *Earth Planet. Sci. Lett.* 396, 213–
787 222. <https://doi.org/10.1016/j.epsl.2014.04.021>

788 Lyle, M., Heath, G.R., Robbins, J.M., 1984. Transport and release of transition
789 elements during early diagenesis: Sequential leaching of sediments from
790 MANOP Sites M and H. Part I. pH 5 acetic acid leach. *Geochim. Cosmochim.*
791 *Acta* 48, 1705–1715. [https://doi.org/10.1016/0016-7037\(84\)90026-7](https://doi.org/10.1016/0016-7037(84)90026-7)

792 Manheim, F.T., Lane-Bostwick, C., 1991. Chemical composition of ferromanganese
793 crusts in the world ocean: a review and comprehensive chemical composition of
794 ferromanganese crusts in the world ocean: a review and comprehensive database.
795 Woods Hole, MA.

796 Merrot, P., Juillot, F., Noël, V., Lefebvre, P., Brest, J., Menguy, N., Guigner, J.M.,
797 Blondeau, M., Viollier, E., Fernandez, J.M., Moreton, B., Bargar, J.R., Morin, G.,
798 2019. Nickel and iron partitioning between clay minerals, Fe-oxides and Fe-
799 sulfides in lagoon sediments from New Caledonia. *Sci. Total Environ.* 689,
800 1212–1227. <https://doi.org/10.1016/j.scitotenv.2019.06.274>

801 Morford, J.L., Emerson, S., 1999. The geochemistry of redox sensitive trace metals in
802 sediments. *Geochim. Cosmochim. Acta* 63, 1735–1750.
803 [https://doi.org/10.1016/S0016-7037\(99\)00126-X](https://doi.org/10.1016/S0016-7037(99)00126-X)

804 Ohnemus, D.C., Rauschenberg, S., Cutter, G.A., Fitzsimmons, J.N., Sherrell, R.M.,
805 Twining, B.S., 2017. Elevated trace metal content of prokaryotic communities
806 associated with marine oxygen deficient zones. *Limnol. Oceanogr.* 62, 3–25.
807 <https://doi.org/10.1002/lno.10363>

808 Palenik, B., Brahamsha, B., Larimer, F.W., Land, M., Hauser, L., Chain, P., Lamerdin,
809 J., Regala, W., Allen, E.E., McCarren, J., Paulsen, I., Dufresne, A., Partensky, F.,
810 Webb, E.A., Waterbury, J., 2003. The genome of a motile marine
811 *Synechococcus*. *Nature*. <https://doi.org/10.1038/nature01943>

812 Peacock, C.L., Sherman, D.M., 2007a. Crystal-chemistry of Ni in marine
813 ferromanganese crusts nodules. *Am. Mineral.* 92, 1087–1092.
814 <https://doi.org/10.2138/am.2007.2378>

815 Peacock, C.L., Sherman, D.M., 2007b. Sorption of Ni by birnessite: Equilibrium
816 controls on Ni in seawater. *Chem. Geol.* 238, 94–106.
817 <https://doi.org/10.1016/j.chemgeo.2006.10.019>

818 Poulson Brucker, R.L., McManus, J., Severmann, S., Berelson, W.M., 2009.
819 Molybdenum behavior during early diagenesis: Insights from Mo isotopes.
820 *Geochemistry, Geophys. Geosystems* 10. <https://doi.org/10.1029/2008GC002180>

821 Price, N.M., Morel, F.M.M., 1991. Colimitation of phytoplankton growth by nickel

822 and nitrogen. *Limnol. Oceanogr.* <https://doi.org/10.4319/lo.1991.36.6.1071>

823 Ragsdale, S.W., 2009. Nickel-based enzyme systems. *J. Biol. Chem.* 284, 18571–
824 18575. <https://doi.org/10.1074/jbc.R900020200>

825 Ratié, G., Garnier, J., Calmels, D., Vantelon, D., Guimarães, E., Monvoisin, G.,
826 Nouet, J., Ponzevera, E., Quantin, C., 2018. Nickel distribution and isotopic
827 fractionation in a Brazilian lateritic regolith: Coupling Ni isotopes and Ni K-edge
828 XANES. *Geochim. Cosmochim. Acta* 230, 137–154.
829 <https://doi.org/10.1016/j.gca.2018.03.026>

830 Rehkämper, M., Nielsen, S.G., 2004. The mass balance of dissolved thallium in the
831 oceans. *Mar. Chem.* 85, 125–139. <https://doi.org/10.1016/j.marchem.2003.09.006>

832 Rudnick, R.L., Gao, S., 2003. 3.01 - Composition of the Continental Crust. *Treatise on*
833 *Geochemistry* 1, 1–64. [https://doi.org/http://dx.doi.org/10.1016/B0-08-043751-](https://doi.org/http://dx.doi.org/10.1016/B0-08-043751-6/03016-4)
834 [6/03016-4](https://doi.org/http://dx.doi.org/10.1016/B0-08-043751-6/03016-4)

835 Sorensen, J. V., Gueguen, B., Stewart, B.D., Peña, J., Rouxel, O., Toner, B.M., 2020.
836 Large nickel isotope fractionation caused by surface complexation reactions with
837 hexagonal birnessite. *Chem. Geol.* 119481.
838 <https://doi.org/10.1016/J.CHEMGEO.2020.119481>

839 Spivak-Birndorf, L.J., Wang, S.J., Bish, D.L., Wasylenki, L.E., 2018. Nickel isotope
840 fractionation during continental weathering. *Chem. Geol.*
841 <https://doi.org/10.1016/j.chemgeo.2017.11.028>

842 Stumm, W., Morgan, J.J., 1996. Metal Ions in Aqueous Solutions: Aspects of
843 Coordination Chemistry, in: *Aquatic Chemistry: Chemical Equilibria and Rates*
844 *in Natural Waters.*

845 Takano, S., Liao, W.H., Tian, H.A., Huang, K.F., Ho, T.Y., Sohrin, Y., 2020. Sources
846 of particulate Ni and Cu in the water column of the northern South China Sea:
847 Evidence from elemental and isotope ratios in aerosols and sinking particles.
848 *Mar. Chem.* 219, 103751. <https://doi.org/10.1016/j.marchem.2020.103751>

849 Takano, S., Tanimizu, M., Hirata, T., Shin, K.C., Fukami, Y., Suzuki, K., Sohrin, Y.,
850 2017. A simple and rapid method for isotopic analysis of nickel, copper, and zinc
851 in seawater using chelating extraction and anion exchange. *Anal. Chim. Acta*
852 967, 1–11. <https://doi.org/10.1016/j.aca.2017.03.010>

853 Tripathy, S.S., Kanungo, S.B., 2005. Adsorption of Co²⁺, Ni²⁺, Cu²⁺ and Zn²⁺ from
854 0.5 M NaCl and major ion sea water on a mixture of δ-MnO₂ and amorphous
855 FeOOH. *J. Colloid Interface Sci.* 284, 30–38.

856 <https://doi.org/10.1016/j.jcis.2004.09.054>

857 Twining, B.S., Baines, S.B., Vogt, S., Nelson, D.M., 2012. Role of diatoms in nickel
858 biogeochemistry in the ocean. *Global Biogeochem. Cycles* 26, 1–9.
859 <https://doi.org/10.1029/2011GB004233>

860 Vance, D., Little, S.H., Archer, C., Cameron, V., Andersen, M.B., Rijkenberg, M.J.A.,
861 Lyons, T.W., 2016. The oceanic budgets of nickel and zinc isotopes: the
862 importance of sulfidic environments as illustrated by the Black Sea. *Philos.*
863 *Trans. R. Soc. A Math. Phys. Eng. Sci.* 374, 20150294.
864 <https://doi.org/10.1098/rsta.2015.0294>

865 Wang, R.M., Archer, C., Bowie, A.R., Vance, D., 2018. Zinc and nickel isotopes in
866 seawater from the Indian Sector of the Southern Ocean: The impact of natural
867 iron fertilization versus Southern Ocean hydrography and biogeochemistry.
868 *Chem. Geol.* 1–13. <https://doi.org/10.1016/j.chemgeo.2018.09.010>

869 Wang, S.J., Rudnick, R.L., Gaschnig, R.M., Wang, H., Wasylenki, L.E., 2019.
870 Methanogenesis sustained by sulfide weathering during the Great Oxidation
871 Event. *Nat. Geosci.* 12. <https://doi.org/10.1038/s41561-019-0320-z>

872 Wang, S.J., Wasylenki, L.E., 2017. Experimental constraints on reconstruction of
873 Archean seawater Ni isotopic composition from banded iron formations.
874 *Geochim. Cosmochim. Acta* 206, 137–150.
875 <https://doi.org/10.1016/j.gca.2017.02.023>

876 Wasylenki, L.E., Howe, H.D., Spivak-Birndorf, L.J., Bish, D.L., 2015. Ni isotope
877 fractionation during sorption to ferrihydrite: Implications for Ni in banded iron
878 formations. *Chem. Geol.* 400, 56–64.
879 <https://doi.org/10.1016/j.chemgeo.2015.02.007>

880 Wegorzewski, A. V., Grangeon, S., Webb, S.M., Heller, C., Kuhn, T., 2020.
881 Mineralogical transformations in polymetallic nodules and the change of Ni, Cu
882 and Co crystal-chemistry upon burial in sediments.
883
884
885
886
887

Table 2[Click here to download Table: Table 2_P.docx](#)**Table 2.** Mn-rich sediments analysed in this study and their Ni isotope compositions. Other sample details: depth in sediment, XRD (for MANOP) or identified MnOx phase (Mn nodules) selected elemental concentrations (for full list, see Table S2), Ni/Al ratios and Ni enrichment factors (where $EF = (Ni/Al)_{sample} / (Ni/Al)_{UCC}$).

	Depth (cm)	XRD analysis?	Mn (wt%)	Fe (wt%)	P (wt%)	Al (wt%)	Ni (µg/g)	Ni/Al	Ni EF	δ⁶⁰Ni	2σ	
MANOP Site H sediments												
VULCAN 37BC MP8950 AAZ	3 - 4 cm	✓	4.77	4.08	0.14	5.27	872	0.017	54	-0.17	0.04	
VULCAN 37BC MP5306 AAZ	5 - 7 cm		4.42	4.23	0.15	5.41	892	0.016	54	-0.18	0.05	
<i>Repeat</i>										-0.24	0.03	
VULCAN 37BC MP5307 AAZ	7 - 9 cm	✓	5.34	4.15	0.14	5.29	785	0.015	49	-0.21	0.04	
VULCAN 37BC MP5310 AAZ	13 - 15 cm		2.12	3.75	0.13	4.80	379	0.008	26	-0.27	0.05	
VULCAN 37BC MP5312 AAZ	17 - 19 cm		2.12	3.99	0.15	5.17	382	0.007	24	-0.29	0.06	
<i>Repeat</i>										-0.28	0.05	
VULCAN 37BC MP5313 AAZ	19 -21 cm	✓	2.09	3.99	0.15	5.26	379	0.007	24	-0.26	0.03	
MANOP Site M sediments												
PLUTO 20BC MP8966 AAZ	0.5 - 1 cm		1.43	5.45	0.12	4.16	286	0.007	23	-0.42	0.04	
PLUTO 20BC MP8967 AAZ	1 - 3 cm	✓	1.65	5.92	0.13	4.69	317	0.007	22	-0.46	0.04	
PLUTO 20BC MP8969 AAZ	5 - 7 cm		1.27	5.30	0.12	4.19	256	0.006	20	-0.43	0.04	
PLUTO 20BC MP8971 AAZ	9 - 11 cm		0.85	5.40	0.11	4.23	228	0.005	18	-0.63	0.04	
PLUTO 20BC MP8975 AAZ	17 - 19 cm		0.12	5.35	0.09	4.11	229	0.006	18	-0.79	0.05	
Mn Nodules												
	Depth (cm)	Main MnOx phase										
USGS NodA1	Surface	Phyllomanganates		19.8	9.75	0.45	1.63	5732	0.352	1153	1.06	0.02*
USGS NodP1	Surface	Phyllomanganates		30.1	4.91	0.16	1.36	11559	0.850	2784	0.34	0.05*
21KG-1n	Surface	Phyllomanganates		31.6	4.29	0.11	1.57	11000	0.790	2587	0.28	0.03
77BC-6	Shallow buried	Todorokite		48.2	0.62	0.05	0.67	1884	0.793	2599	-0.22	0.04
22KL-530cm	Buried, 530cm	Todorokite		31.7	3.23	0.09	1.83	10328	0.452	1482	-0.08	0.04
22KL-801cm	Buried, 801cm	Todorokite		31.9	3.37	0.09	2.03	11492	0.351	1150	0.01	0.03

*n = 5, 2 SD